Received: 30 May 2024 | Revised: 16 September 2024 | Accepted: 17 September 2024

DOI: 10.1002/pamm.202400173

RESEARCH ARTICLE

On the application of the finite cell method to static analysis of trabecular bone tissue specimen using high-resolution microCT data

Mohammad Amin Shahmohammadi[1] | **Imke Fiedler**[2] | **Annika vom Scheidt**[3] | **Björn Busse**[2] | **Alexander Düster**[1]

[1]Numerical Structural Analysis with Application in Ship Technology, Institute for Ship Structural Design and Analysis (M-10), Hamburg University of Technology, Hamburg, Germany

[2]Department of Osteology and Biomechanics, University Medical Center Hamburg-Eppendorf, Hamburg, Germany

[3]Division of Macroscopic and Clinical Anatomy, Gottfried Schatz Research Center, Medical University of Graz, Graz, Austria

Correspondence
Mohammad Amin Shahmohammadi, Numerical Structural Analysis with Application in Ship Technology, Institute for Ship Structural Design and Analysis (M-10), Hamburg University of Technology, Hamburg, Germany.
Email: ma.shahmohammadi@tuhh.de

Funding information
Alexander von Humboldt Foundation: Georg Forster Research Fellowship Program for Post-docs

Abstract

This study aims to introduce a robust numerical approach to simulate complex small-scale mediums such as trabecular bone tissue in form of a cylindrical specimen taken from human vertebra. Consideration of previous related studies indicates that there are several challenges in utilizing standard finite element (FE) techniques for the analysis of such biomechanical structures. This is mainly due to their time-consuming procedure required for generating geometry conforming meshes. In this regard, the finite cell method (FCM) is an interesting alternative because it is based on the concept of the fictitious domain technique in which underlying meshes do not need to conform to the boundary of the domain. Since the considered trabecular bone tissue consists of a complex small-scale internal morphology, generating a FE mesh is rather complicated. So, the application of the FCM can be justified by overcoming the mentioned shortcomings of FE methods for this problem. Using FCM, it is possible to simulate the mentioned trabecular cylinder from vertebral body using higher order cells of regular shapes where the geometry is taken care of through the numerical integration. The input for the present numerical tool corresponding to the complex internal morphology of the proposed tissue is given by a high-resolution microCT scan. The outcome of the FCM will be compared to results obtained by mechanical testing of the specimen.

1 | INTRODUCTION

Reducing the risk of fractures caused by osteoporosis, particularly in the elderly, stands as a paramount objective within the realm of orthopedics. Numerous efficacious treatment options exist for osteoporosis and clinical imaging, for example, based on high-resolution peripheral quantitative CT (HR-pQCT) allows to assess changes in bone density and architecture over the time. However, a crucial consideration of this issue involves assessing the treatment's effectiveness across trabecular bone from various regions within a whole bone, for example, a vertebral body. The primary approach in this

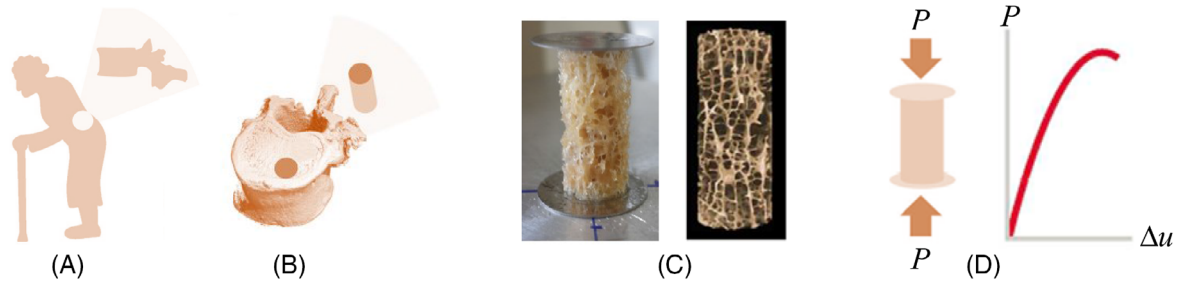

FIGURE 1 A schematic view of the geometrical characteristics of the considered bone core and the relevant experimental procedure [1].

context involves experimental investigations [1–3]. In this context, computational biomechanical approaches offer the unique opportunity to systematically simulate the effect of altered tissue architectures on the mechanical properties of bone at different length scales. The finite element method (FEM) stands as the predominant numerical technique utilized for simulating bones and vertebrae based on CT scan data. For instance, FEM was utilized to model the human vertebrae on macro-scale for various biomechanical aspects [4–7]. However, a noteworthy point in these studies is assuming the vertebrae as continuous mediums devoid of porosity, whereas in reality, vertebrae contain pores of different sizes and highly complex internal morphology. In such a problem, the discretization process for FEM becomes exceedingly complex and, at times, unfeasible [8]. For problems involving complex geometries, meshless and meshfree methods [9, 10], as well as the virtual element method [11] are alternative discretization schemes. In this work, we follow the idea of fictitious domain methods. This approach led to the development and adoption of the finite cell method (FCM), which has been utilized in numerous numerical simulations to incorporate intricate morphological features [12, 13]. To address the complexity of discretization in such problems, FCM allows for the embedding of complex geometries, which can be discretized using simple-shaped elements and a special integration scheme enables the representation of the intricate morphology in the physical domain. Several integration schemes for FCM are available in the literature such as recursive octree subdivision [14], voxel-based subdivision [15], moment fitting [16], and non-negative moment fitting [17].

In the numerical simulation of trabecular bone tissues, a critical aspect is the characterization of their mechanical properties. Previous research suggests that an effective strategy involves converting microCT data into mechanical parameters. One of the most suitable approaches is to utilize Hounsfield units (HUs), a quantitative scale used to describe radio-density [18–21].

In this study, we aim to conduct numerical simulations of a trabecular bone tissue specimen featuring intricate microarchitecture using the FCM. The specimen has undergone experimental testing under incremental compressive loading. The numerical modeling inputs comprise a vast array of microCT images obtained from this cylindrical specimen, drilled from a human vertebra.

The significance of the present work in employing voxel-based FCM lies in its reduction of the required number of discretizations for biomechanical problems compared to voxel-based micro FEM. In voxel-based micro FEM for the analysis of trabecular bone tissues, each voxel is treated as a single finite element (FE) [22–24]. In contrast, voxel-based FCM allows for several voxels to be included in a single finite cell, eliminating nonphysical voxels during integration procedure based on the concept of a fictitious domain. This approach reduces the number of degrees of freedom (DOF) needed to achieve accurate results.

2 | DESCRIPTION OF THE EXPERIMENTAL SPECIMEN

2.1 | Cylindrical trabecular bone core

The experimental specimen in the present study incorporates a cylindrical trabecular bone core drilled from the L3-type vertebrae of an elderly osteoporotic woman. During the experimental procedure, the specimen underwent quasi-static uni-axial compressive loading to achieve its load-displacement curve. The diameter and height of the specimen are 9.15 and 20.2 mm, respectively. Figure 1 illustrates the geometrical characteristics of the specimen under consideration, along with the associated experimental procedure.

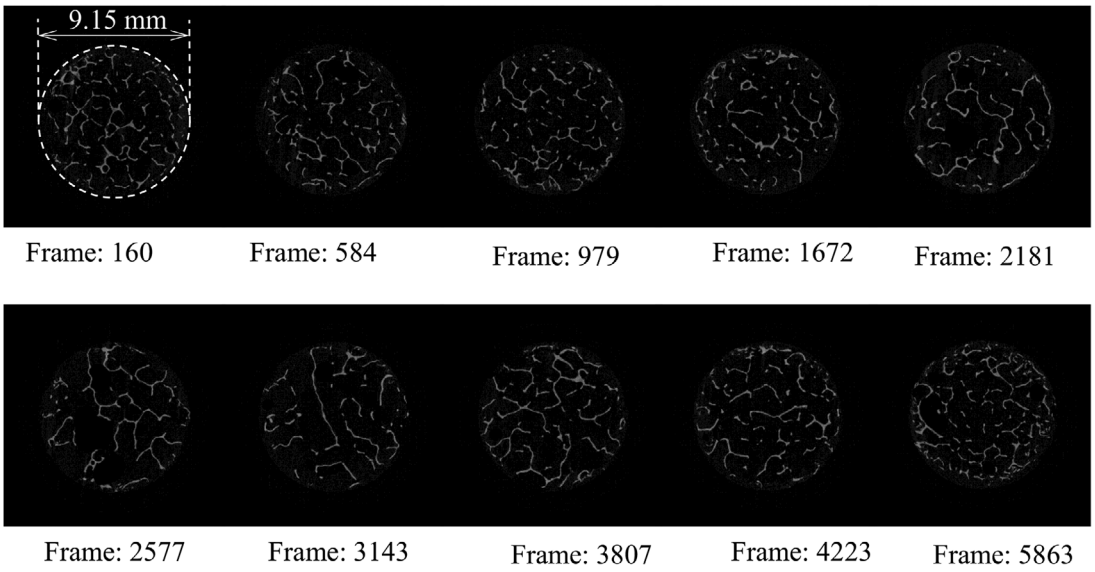

FIGURE 2 The high-resolution images related to various frames of the microCT scanning process.

2.2 | The microCT procedure

The introduced trabecular bone sample underwent microCT scanning, resulting in 6575 frames (Skyscan 1272, Bruker, Kontich, Belgium). Briefly, scans were acquired at an acceleration voltage of 80 kV, source current of 125 μA, isometric voxel size of 3.5 μm, and with a 0.5-mm aluminum filter. Each frame captured an image comprising 4025 × 4025 pixels. Due to the large number of frames, we present a selection of 10 images from various frames of the scanning process in Figure 2 as examples.

3 | VOXEL-BASED NUMERICAL METHOD

In this study, we conduct numerical simulations based on voxel models. The voxel model is equipped with HUs, which allow us to distinguish between the fictitious and physical domains. Furthermore, from the HUs, we can estimate the mechanical properties of the bone, as explained in the next subsection.

3.1 | Mechanical characteristics

The mechanical properties of the proposed trabecular bone tissue specimen, being a nonhomogeneous material, are specified for each voxel based on its HU value (HU). Extracting this value for each voxel from the high-resolution microCT images is crucial. In this context, the image data (ID) representing the gray value of each voxel are accessible, where pure black and pure white correspond to 0 and 255, respectively. Notably, the microCT scans included regions, which only contained water and air, allowing for the conversion of gray values of images to HUs.

To elucidate the above explanations, let us consider a microCT image that has been meshed by rectangular finite cells, as shown in Figure 3A. By focusing on a specific cell, as depicted in Figure 3B, we can observe the ID values based on the colors of pixels within this region, as illustrated in Figure 3C.

The previous related publications [18–20] suggest that there exists a linear relationship between the values of image data and HUs as follows:

$$HU = \frac{HU_{max} - HU_{min}}{ID_{max} - ID_{min}}(ID - ID_{min}) + HU_{min} \tag{1}$$

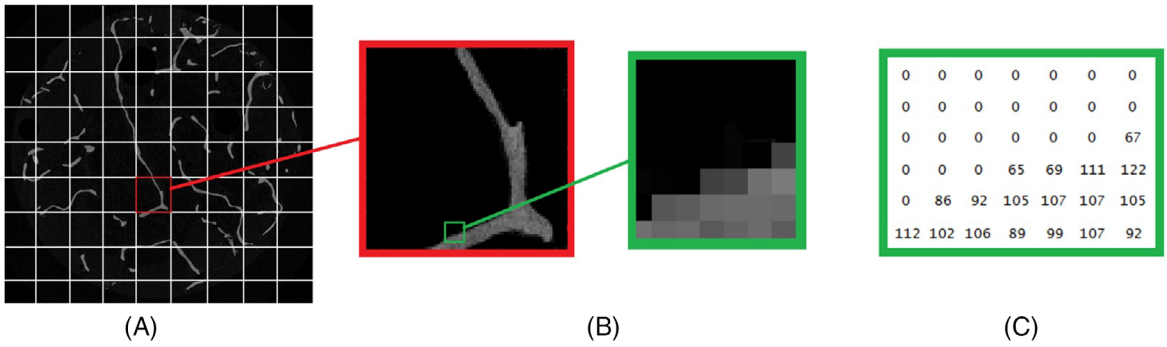

FIGURE 3 *ID* values of microCT image based on the colors of pixels.

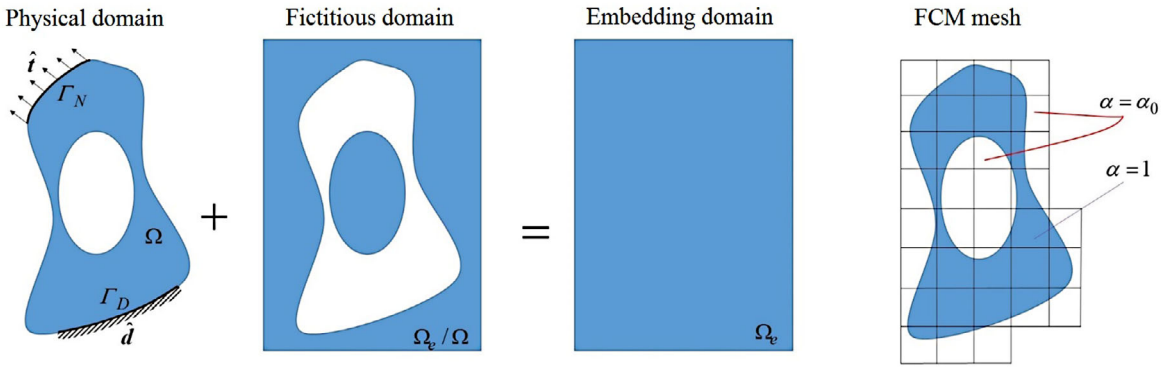

FIGURE 4 A schematic description of physical, fictitious, and embedding domains together with the FCM discretization.

where $HU_{min}, HU_{max}, ID_{min}$, and ID_{max} are the minimum and maximum values of Hounsfield units and image data, respectively.

With the obtained HU values for each pixel according to Equation (1), the Young's modulus (E) can be calculated for each pixel in terms of the corresponding HU. In this context, the following function, proposed in ref. [21] based on several experiments, can be utilized:

$$E(HU) = 0.06(0.916HU + 114)^{1.51} \tag{2}$$

3.2 | Finite cell method

The FCM has been developed based on the fictitious domain approach, combined with higher-order versions of the FEM. Its efficiency in the present study lies in the fact that in FCM, only the embedding domain needs to be meshed with simply shaped elements/cells, even when the existing geometry is highly complex. The mentioned efficiency is schematically illustrated in Figure 4. The parameter α in the figure is defined to differentiate between the physical and fictitious domains within the embedded domain. Specifically, in the physical domain, $\alpha = 1$, whereas in the fictitious domain, $\alpha = \alpha_0$. Theoretically, α_0 should be equal to 0; however, to avoid conditioning problems in numerical computations, it is not considered exactly equal to 0. Therefore, in the present work, it is assumed that $\alpha_0 = 10^{-6}$.

Based on the previous explanations regarding the coefficient α and its application in FCM, the stiffness matrix for a generic finite cell, denoted by the superscript c, can be expressed as follows:

$$\mathbf{K}^{(c)} = \int_{\Omega^{(c)}} \mathbf{B}^T \alpha \mathbf{D}^{(c)} \mathbf{B} \, d\Omega^{(c)} = \int_{-1}^{1}\int_{-1}^{1}\int_{-1}^{1} \mathbf{B}^T \alpha \mathbf{D}^{(c)} \mathbf{B} \, det\left(\mathbf{J}^{(c)}\right) d\xi d\eta d\zeta \tag{3}$$

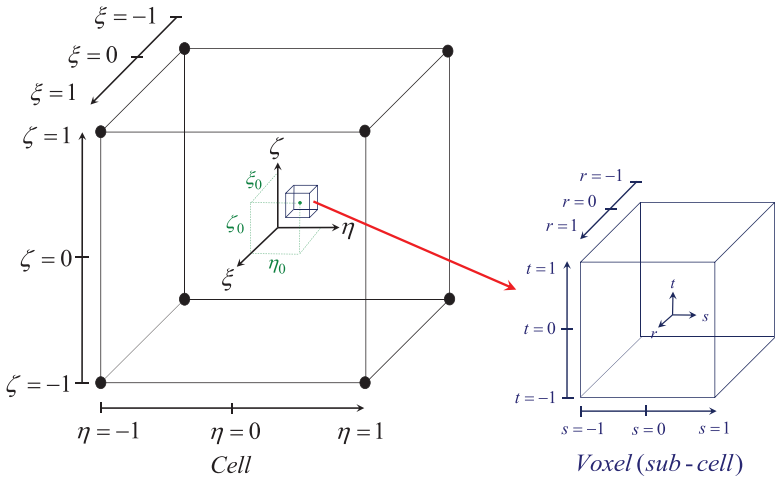

FIGURE 5 Graphical description of the local coordinate systems of a cell (ξ, η, ζ) and a generic subcell inside it (r, s, t).

in which the isotropic elasticity matrix of the cell c reads

$$\mathbf{D}^{(c)} = \frac{\nu^{(c)}E^{(c)}}{(1+\nu^{(c)})(1-2\nu^{(c)})}\overline{\mathbf{D}}_1 + \frac{E^{(c)}}{2(1+\nu^{(c)})}\overline{\mathbf{D}}_2,$$

$$\overline{\mathbf{D}}_1 = \begin{bmatrix} \mathbf{I}^t_{3\times3} & \mathbf{0}_{3\times3} \\ \mathbf{0}_{3\times3} & \mathbf{0}_{3\times3} \end{bmatrix}, \ \overline{\mathbf{D}}_2 = \begin{bmatrix} 2\mathbf{I}^d_{3\times3} & \mathbf{0}_{3\times3} \\ \mathbf{0}_{3\times3} & \mathbf{I}^d_{3\times3} \end{bmatrix}, \ \mathbf{I}^t_{3\times3} = \begin{bmatrix} 1 & 1 & 1 \\ 1 & 1 & 1 \\ 1 & 1 & 1 \end{bmatrix}, \ \mathbf{I}^d_{3\times3} = \begin{bmatrix} 1 & 0 & 0 \\ 0 & 1 & 0 \\ 0 & 0 & 1 \end{bmatrix} \tag{4}$$

3.3 | Numerical integration strategy

An important ingredient of the FCM discretization is the three-dimensional numerical integration in Equation (3). Generally, in FCM, the integration strategy involves dividing the integration domain of the cell into subcells, ensuring that only the subcells of the physical domain are considered in the integration process.

In this study, a voxel-based strategy is adopted for integration, where each voxel is considered as a subcell equipped with a local coordinate system (r, s, t). Considering that each frame of the microCT image incorporates $n_x \times n_y$ pixels and that there are n_z frames in the microCT scan, the embedded region is defined by $n_x \times n_y \times n_z$ voxels. Moreover, the embedding domain is discretized into $N_x \times N_y \times N_z$ cells, each of which incorporates $n^c_x \times n^c_y \times n^c_z$ voxels, where $n^c_x = n_x/N_x$, $n^c_y = n_y/N_y$, and $n^c_z = n_z/N_z$ represent the number of voxels in the x, y, and z directions of the cell, respectively. Considering a generic voxel (subcell) within a cell (Figure 5), where the location of its center in the ξ, η, ζ coordinate system is denoted as (ξ_0, η_0, ζ_0), the relationship between the components of the cell's and voxel's local coordinate systems can be expressed as follows:

$$\xi = \xi_0 + \frac{r}{n^c_x}, \quad \eta = \eta_0 + \frac{s}{n^c_y}, \quad \zeta = \zeta_0 + \frac{t}{n^c_z} \tag{5}$$

Therefore, based on the defined voxel's local coordinate system in Figure 5 and Equation (5) utilizing the Gauss quadrature method, the voxel-based numerical integration of the stiffness matrix in Equation (3) can be expressed as follows:

$$\begin{aligned} \mathbf{K}^{(c)} &= \sum_{k=1}^{n^c_z}\sum_{j=1}^{n^c_y}\sum_{i=1}^{n^c_x}\mathbf{K}^{(ijk)} = \sum_{k=1}^{n^c_z}\sum_{j=1}^{n^c_y}\sum_{i=1}^{n^c_x}\left(\int_{-1}^{1}\int_{-1}^{1}\int_{-1}^{1}\left(\mathbf{B}^{(ijk)}\right)^T\alpha\mathbf{D}^{(ijk)}\mathbf{B}^{(ijk)}det\left(\mathbf{J}^{(ijk)}\right)det\left(\overline{\mathbf{J}}^{(ijk)}\right)drdsdt\right) \\ &= \sum_{k=1}^{n^c_z}\sum_{j=1}^{n^c_y}\sum_{i=1}^{n^c_x}\left(\sum_{n=1}^{n^{gp}_t}\sum_{m=1}^{n^{gp}_s}\sum_{l=1}^{n^{gp}_r}\left(\mathbf{B}^{(ijk)}_{lmn}\right)^T\alpha\mathbf{D}^{(ijk)}\mathbf{B}^{(ijk)}_{lmn}det\left(\mathbf{J}^{(ijk)}_{lmn}\right)det\left(\overline{\mathbf{J}}^{(ijk)}_{lmn}\right)w^r_l w^s_m w^t_n\right) \end{aligned} \tag{6}$$

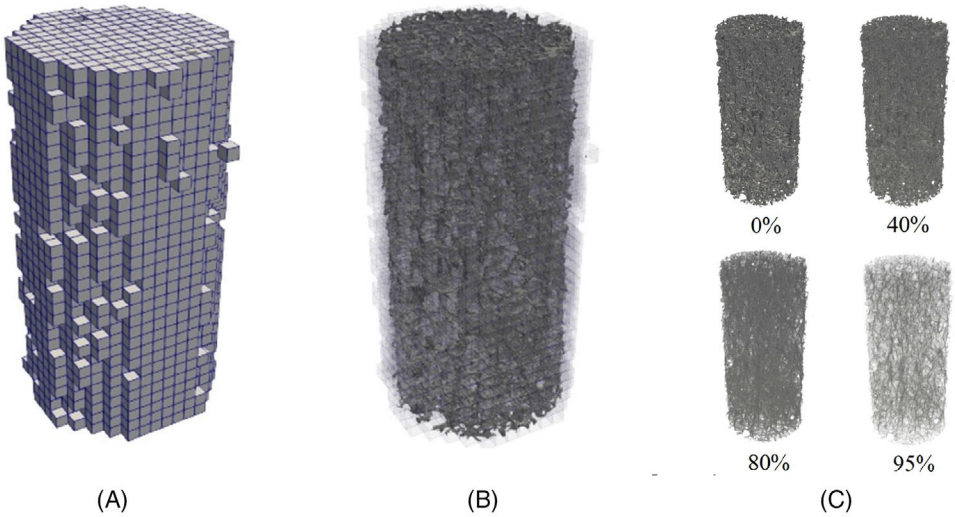

FIGURE 6 A graphical view of the trabecular bone tissue discretization $N_x \times N_x \times N_x = 20 \times 20 \times 31$ incorporating (A) active cells, (B) achieved complex morphology by eliminating the fictitious domain, and (C) its view in different transparencies.

in which n_r^{gp}, n_s^{gp}, and n_t^{gp} are the number of Gaussian integration points through the r, s, and t directions, respectively, and the parameters w_l^r, w_m^s, and w_n^t are their corresponding integration weights. Assuming that the exact geometry is defined by the voxel representation, numerical integration can be performed exactly. This is due to the fact that the corresponding mapping functions of the cell and subcell result in constant Jacobians, leading to a polynomial integrand that can be evaluated exactly using Gaussian quadrature. The volume fraction of the broken cell, that is, the ratio of material-occupied volume to the cell's volume, has no influence on the integration error. However, the volume fraction of the entire cell significantly affects the condition number of the resulting equation system. To address this issue, a stabilization method for improving the condition number of the equation system has been presented in Garhuom et al. [25].

4 | NUMERICAL RESULTS

In this section, the results of the FCM simulation of the trabecular bone tissue depicted in Figure 1 will be presented. An important consideration arises due to the large number of voxels resulting from the current microCT scanning process, which involves 6575 frames, thus generating 6575 high-resolution images (4025×4025 pixels each). Consequently, the geometry of the simulated tissue is defined by $4025 \times 4025 \times 6575$ voxels, demanding a substantial amount of memory. To address this shortcoming, we mitigated it by reducing the resolution of the images to 300×300 pixels and by eliminating several frames of similar images from the scanning process. Consequently, we achieved a substantial reduction in the number of voxels, resulting in a geometry defined by $300 \times 300 \times 372$ voxels, each of which incorporates Hounsfield units (HU), coefficient α and its location in the defined coordinate system.

In the subsequent step, the geometry defined by the aforementioned voxels has been discretized using simple second-order brick elements/cells. It is worth noting that during the integration process, any cells where all the voxels belong to fictitious domain ($\alpha = \alpha_0$) are rendered inactive. Figure 6 provides a detailed graphical description of the internal structure of the trabecular bone tissue, emphasizing its active elements based on a $N_x \times N_y \times N_z = 20 \times 20 \times 31$ discretization while excluding the fictitious domain. Furthermore, to attain converged results, various discretizations of the proposed tissue using the second-order brick elements/cells have been explored, as illustrated in Figure 7.

The next phase of the study involves a convergence analysis of the linear behavior of the proposed trabecular bone tissue. As the study is limited to the linear static response of the tissue under axial compressive load, we focus solely on the linear portion of the load–displacement curve obtained from experimental tests. This portion is characterized by defining the equivalent compressive stiffness (k) of the tissue, which is determined by the slope of the tangential line to this part of the curve. In Table 1, the achieved values of compressive stiffness corresponding to each discretization are expressed and then compared with the experimental data. This comparison acceptable accuracy and reliability of the present computational tool in simulating the linear elastic behavior of the proposed biomechanical structure.

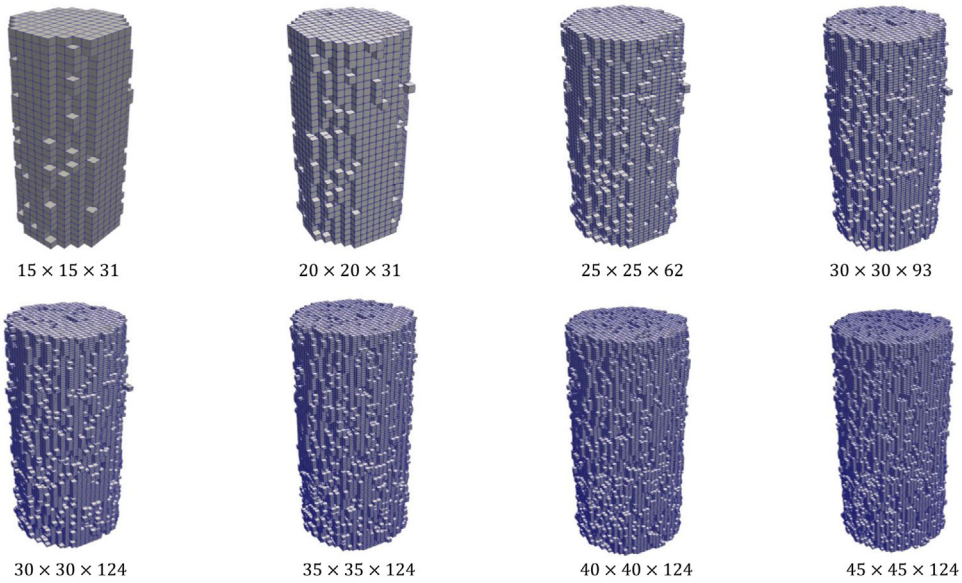

FIGURE 7 Various discretizations of the trabecular bone tissue by the second-order brick elements/cells.

TABLE 1 Convergence study and comparing the achieved compressive stiffness (k) by numerical simulation and experimental study.

$N_x \times N_y \times N_z$	k(N/μm)	DOF	N.N.Z.[a]	T.N.C.[b]	N.A.C.[c]
15 × 15 × 31	0.7761	81 675	1.41×10^7	6975	2951
20 × 20 × 31	0.6806	132 246	2.31×10^7	12 400	4830
25 × 25 × 62	0.5080	372 114	6.35×10^7	38 750	13 114
30 × 30 × 93	0.4422	736 770	1.22×10^8	83 700	24 754
30 × 30 × 124	0.4276	960 732	1.57×10^8	111 600	31 905
35 × 35 × 124	0.3894	1 218 345	1.95×10^8	151 900	39 293
40 × 40 × 124	0.3670	1 489 677	2.34×10^8	198 400	46 755
45 × 45 × 124	0.3540	1 774 125	2.76×10^8	251 100	54 789
46 × 46 × 124	0.3510	1 827 906	2.83×10^8	262 384	56 181
Experimental	0.3179	–	–	–	–

[a]Number of nonzero elements of the stiffness matrix.
[b]Total number of cells.
[c]Number of active cells.

To analyze the convergence trend in detail, Figure 8 plots compressive stiffness against the number of DOF.

In Figure 8, the convergence trend in Stage 1 corresponds to the increase in discretization along the z direction from 93 to 124, while maintaining the fixed discretization of 30 along the x and y directions. This suggests that a z-direction discretization of 124 is adequate. Therefore, to achieve converged results, it is necessary to increase the discretization along the x and y directions. Consequently, Stage 2 demonstrates that increasing the discretization along the x and y directions from 45 to 46, while maintaining a fixed discretization of 124 along the z direction, yields no significant change in the results.

The numerical investigations are continued by comparing the load–displacement relationships obtained from experimental studies with those from numerical simulations, as illustrated in Figure 9. It is noteworthy that the curve representing experimental studies in this figure include both linear elastic and nonlinear behavior, whereas the present simulation is limited to linear elastic analysis. Therefore, our focus is primarily on the linear elastic part of the load–displacement curve, where nonlinear behavior is not significant, as indicated by the green line. The presented results in Figure 9 exhibit an acceptable accuracy of the present numerical simulation as compared with the experimental results ($Error = 10.3\%$).

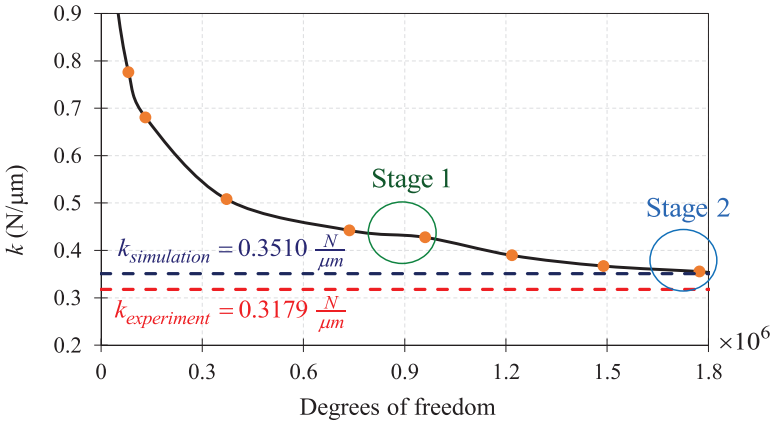

FIGURE 8 Convergence trend of the compressive stiffness k (N/μm) respect to increase of the number of degrees of freedom.

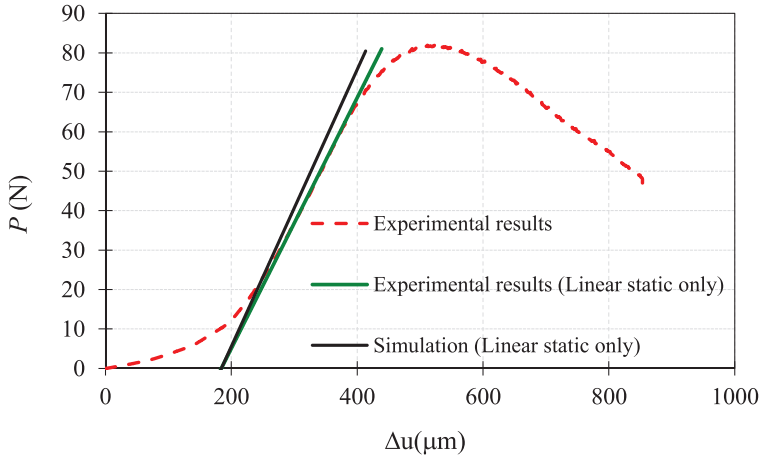

FIGURE 9 Comparative investigation of load–displacement relationship: numerical simulations versus experimental studies.

Further investigations pertain to the distribution contours of stress and displacement magnitudes throughout the proposed trabecular tissue. These contours are depicted in Figure 10, showing the stress distribution in two different section views. The graphical results in Figure 10 illustrate that using FCM with the normal discretizations depicted in Figure 7, a trabecular bone tissue with highly intricate internal morphology can be analyzed with a good level of accuracy.

Beside the advantages of the present work, it has some limitations. The present method has been applied to the analysis of only one sample and has not been tested on additional cases to evaluate its effectiveness in greater detail. Due to limited memory for numerical analyses, we had to coarsen the resolution of microCT images, which may introduce some errors in the results. In the present study, the relationship used to characterize the mechanical properties was based on microCT scans with different scan settings, which may also cause some errors in the results.

5 | CONCLUDING REMARKS

In this paper, we introduced a robust numerical approach based on the FCM to simulate trabecular bone tissue in the form of a cylindrical specimen extracted from the human vertebra, incorporating complex internal geometry. By employing the concept of the fictitious domain in FCM, we successfully addressed the challenge of discretizing such a biomechanical structure. This approach enabled us to reduce the time-consuming procedure required for generating geometry-conforming meshes, a common issue encountered in methods like the FEM, while it keeps the accuracy as much as possible.

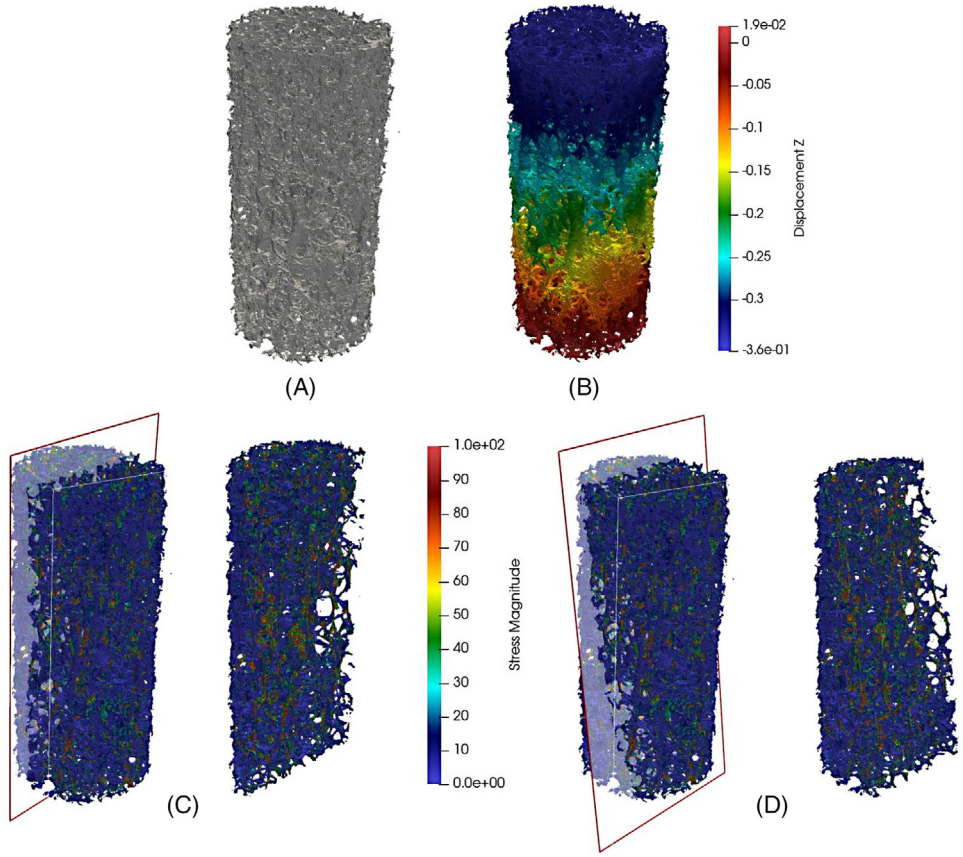

FIGURE 10 Graphical representation of (A) the captured geometry of the trabecular bone tissue, with corresponding contour plots for (B) displacement and stress distribution, shown in (C) vertical and (D) inclined section views, both corresponding to vertical downward displacement $\Delta u = 350\ \mu$m.

Another aspect of the present study was proposing an efficient approach to convert high-resolution microCT images into the initial data including both geometrical and mechanical properties required for the numerical simulation of such a complex biomechanical structure.

By employing a voxel-based integration scheme, we were able to assign various mechanical properties to the voxels. This approach enabled us to consider the heterogeneity of the material, which was derived from the color-based microCT image data.

Finally, the proposed solution was successfully tested by comparing the achieved results with the experimental results approving the accuracy of the present method.

ACKNOWLEDGMENTS

This research received support from the Alexander von Humboldt Foundation (AvH), and the authors would like to express their gratitude for the funding.

Open access funding enabled and organized by Projekt DEAL.

ORCID

Mohammad Amin Shahmohammadi https://orcid.org/0009-0002-0563-5534

REFERENCES

1. vom Scheidt, A., Hemmatian, H., Püschel, K., Krause, M., Amling, M., & Busse, B. (2019). Bisphosphonate treatment changes regional distribution of trabecular microstructure in human lumbar vertebrae. *Bone*, *127*, 482–487.
2. vom Scheidt, A., Seifert, E. F. G., Pokrant, C., Püschel, K., Amling, M., Busse, B., & Milovanovic, P. (2019). Subregional areal bone mineral density (aBMD) is a better predictor of heterogeneity in trabecular microstructure of vertebrae in young and aged women than subregional trabecular bone score (TBS). *Bone*, *122*, 156–165.

3. Rolvien, T., Hahn, M., Siebert, U., Püschel, K., Wilke, H. J., Busse, B., Amling, M., & Oheim, R. (2017). Vertebral bone microarchitecture and osteocyte characteristics of three toothed whale species with varying diving behaviour. *Scientific Reports*, *7*(1), 1604.
4. Zhang, J., Chen, W., Weng, R., Liang, D., Jiang, X., & Lin, H. (2023). Biomechanical effect of endplate defects on the intermediate vertebral bone in consecutive two-level anterior cervical discectomy and fusion: A finite element analysis. *BMC Musculoskeletal Disorders*, *24*(1), 407.
5. Oku, N., Demura, S., Tawara, D., Kato, S., Shinmura, K., Yokogawa, N., Yonezawa, N., Shimizu, T., Kitagawa, R., Handa, M., Ryohei, A., & Tsuchiya, H. (2023). Biomechanical investigation of long spinal fusion models using three-dimensional finite element analysis. *BMC Musculoskeletal Disorders*, *24*(1), 175.
6. Oe, S., Narita, K., Hasegawa, K., Natarajan, R. N., Yamato, Y., Hasegawa, T., Yoshida, G., Banno, T., Arima, H., Mihara, Y., Ushirozako, H., Ide, K., Yamada, T., Watanabe, Y., & Matsuyama, Y. (2023). Longer screws can reduce the stress on the upper instrumented vertebra with long spinal fusion surgery: A finite element analysis study. *Global Spine Journal*, *13*(4), 1072–1079.
7. Huang, S., Zhou, C., & Zhang, X. (2023). Biomechanical analysis of sandwich vertebrae in osteoporotic patients: Finite element analysis. *Frontiers in Endocrinology*, *14*, 1259095.
8. Lacroix, D., Chateau, A., Ginebra, M. P., & Planell, J. A. (2006). Micro-finite element models of bone tissue-engineering scaffolds. *Biomaterials*, *27*(30), 5326–5334.
9. Fornberg, B., & Flyer, N. (2015). *A primer on radial basis functions with applications to the geosciences*. Society for Industrial and Applied Mathematics, SIAM.
10. Chen, J. S., & Belytschko, T. (2015). Meshless and meshfree methods. In B. Engquist (Ed.), *Encyclopedia of applied and computational mathematics* (pp. 886–894). Springer.
11. Wriggers, P., Aldakheel, F., & Hudobivnik, B. (2024). *Virtual element methods in engineering sciences*. Springer.
12. Yang, Z., Ruess, M., Kollmannsberger, S., Düster, A., & Rank, E. (2012). An efficient integration technique for the voxel-based finite cell method. *International Journal for Numerical Methods in Engineering*, *91*(5), 457–471.
13. Ruess, M., Tal, D., Trabelsi, N., Yosibash, Z., & Rank, E. (2012). The finite cell method for bone simulations: Verification and validation. *Biomechanics and Modeling in Mechanobiology*, *11*, 425–437.
14. Düster, A., & Allix, O. (2020). Selective enrichment of moment fitting and application to cut finite elements and cells. *Computational Mechanics*, *65*, 429–450.
15. Yang, Z., Kollmannsberger, S., Düster, A., Ruess, M., Garcia, E. G., Burgkart, R., & Rank, E. (2011). Non-standard bone simulation: Interactive numerical analysis by computational steering. *Computing and Visualization in Science*, *14*, 207–216.
16. Müller, B., Kummer, F., & Oberlack, M. (2013). Highly accurate surface and volume integration on implicit domains by means of moment-fitting. *International Journal for Numerical Methods in Engineering*, *96*(8), 512–528.
17. Garhuom, W., & Düster, A. (2022). Non-negative moment fitting quadrature for cut finite elements and cells undergoing large deformations. *Computational Mechanics*, *70*(5), 1059–1081.
18. Buenger, F., Eckardt, N., Sakr, Y., Senft, C., & Schwarz, F. (2021). Correlation of bone density values of quantitative computed tomography and hounsfield units measured in native computed tomography in 902 vertebral bodies. *World Neurosurgery*, *151*, e599–e606.
19. Buenger, F., Sakr, Y., Eckardt, N., Senft, C., & Schwarz, F. (2021). Correlation of quantitative computed tomography derived bone density values with Hounsfield units of a contrast medium computed tomography in 98 thoraco-lumbar vertebral bodies. *Archives of Orthopaedic and Trauma Surgery*, *142*, 1–6.
20. Hendrickson, N. R., Pickhardt, P. J., Del Rio, A. M., Rosas, H. G., & Anderson, P. A. (2018). Bone mineral density t-scores derived from ct attenuation numbers (Hounsfield units): Clinical utility and correlation with dual-energy x-ray absorptiometry. *The Iowa Orthopaedic Journal*, *38*, 25–31.
21. El-Gizawy, A. S., Ma, X., Pfeiffer, F., Schiffbauer, J. D., & Selly, T. (2023). Characterization of microarchitectures, stiffness and strength of human trabecular bone using micro-computed tomography (micro-ct) scans. *BioMed*, *3*(1), 89–100.
22. Wang, J., Zhou, B., Jenny Hu, Y., Zhang, Z., Eric Yu, Y., Nawathe, S., Nishiyama, K. K., Keaveny, T. M., Shane, E., & Edward Guo, X. (2019). Accurate and efficient plate and rod microfinite element models for whole bone segments based on high-resolution peripheral computed tomography. *Journal of Biomechanical Engineering*, *141*(4), 041005.
23. Niebur, G. L., Feldstein, M. J., Yuen, J. C., Chen, T. J., & Keaveny, T. M. (2000). High-resolution finite element models with tissue strength asymmetry accurately predict failure of trabecular bone. *Journal of Biomechanics*, *33*(12), 1575–1583.
24. Adams, M. F., Bayraktar, H. H., Keaveny, T. M., & Papadopoulos, P. (2004). Ultrascalable implicit finite element analyses in solid mechanics with over a half a billion degrees of freedom. In *SC'04: Proceedings of the 2004 ACM/IEEE conference on supercomputing* (pp. 34–34).
25. Garhuom, W., Usman, K., & Düster, A. (2022). An eigenvalue stabilization technique to increase the robustness of the finite cell method for finite strain problems. *Computational Mechanics*, *69*, 1225–1240.

How to cite this article: Shahmohammadi, M. A., Fiedler, I., vom Scheidt, A., Busse, B., & Düster, A. (2024). On the application of the finite cell method to static analysis of trabecular bone tissue specimen using high-resolution microCT data. *Proceedings in Applied Mathematics and Mechanics*, *24*, e202400173. https://doi.org/10.1002/pamm.202400173